Free-standing porous carbon electrodes derived from wood for high-performance Li-O$_2$ battery applications

Jingru Luo[1,§], Xiahui Yao[1,§], Lei Yang[2,§], Yang Han[2], Liao Chen[2], Xiumei Geng[2], Vivek Vattipalli[3], Qi Dong[1], Wei Fan[3], Dunwei Wang[1] (✉), Hongli Zhu[2] (✉)

[1] *Department of Chemistry, Merkert Chemistry Center, Boston College, 2609 Beacon St., Chestnut Hill, MA 02467 USA*

[2] *Department of Mechanical and Industrial Engineering, Northeastern University, 360 Huntington Avenue, Boston, MA 02115 USA*

[3] *Chemical Engineering Department, University of Massachusetts Amherst, 686 N. Pleasant Street, Amherst, MA 01003 USA*

[§] *Jingru Luo, Xiahui Yao and Lei Yang contributed equally to this work.*

ABSTRACT

Porous carbon materials are widely used in particulate forms for energy applications such as fuel cells, batteries, and (super) capacitors. To better hold the particles together, polymeric additives are utilized as binders, which not only increase the weight and volume of the devices, but also cause adverse side effects. We developed a wood-derived, free-standing porous carbon electrode and successfully applied it as a cathode in Li-O$_2$ batteries. The spontaneously formed hierarchical porous structure exhibits good performance in facilitating the mass transport and hosting the discharge products of Li$_2$O$_2$. Heteroatom (N) doping further improves the catalytic activity of the carbon cathode with lower overpotential and higher capacity. Overall, the Li-O$_2$ battery based on the new carbon cathode affords a stable energy efficiency of 65% and can be operated for 20 cycles at a discharge depth of 70%. The wood-derived free-standing carbon represents a new, unique structure for energy applications.

1 Introduction

Electrode materials with porous structures, particularly the ones with hierarchical pores, are highly coveted for energy applications such as fuel cells [1, 2], batteries [3, 4], and (super) capacitors [5, 6]. Of these, porous carbon is probably the most commonly used material, owing to its relatively high electrical conductivity, good chemical stability, low cost, and non-toxicity [7, 8]. However, most commercially available carbon materials are in particulate form with their typical sizes ranging between nanometers and microns [9], presenting challenges associated with their assembly toward desired connectivity and mechanical strength for practical applications. One of the strategies to overcome this drawback is to introduce polymeric additives as binders to hold the particles together [10]. While widely implemented in many commercially successful systems, such approaches introduce undesirable consequences. For example, the addition of these inactive

materials invariably increases the weight and volume of the devices [11] (e.g., batteries) and complicates the manufacturing process [12]. Moreover, the additives sometimes introduce unexpected side effects that are detrimental to the operation of energy conversion and storage devices [13]. This issue can be particularly acute in emerging technologies such as Li-O$_2$ batteries. For instance, poly(vinylidene difluoride) (PVdF) binder plays a critical role in the success of Li-ion batteries, but it is reportedly unstable with respect to the ubiquitous superoxide species in Li-O$_2$ batteries [14, 15]. Furthermore, there have been studies demonstrating that the binders used in the cathode may limit O$_2$ diffusion by blocking the pores and reducing the active surface area for Li$_2$O$_2$ deposition [16, 17]. These negative issues related to the particulate nature of carbon can in principle be resolved by using free-standing carbon materials that are much larger in their macroscale dimensions but feature pores of similar sizes at the micro and mesoscales [18]. Indeed, efforts in this direction have provided promising preliminary results [19–24]. For instance, Zhang et al. [20] developed a free-standing palladium-modified hollow spherical carbon cathode to endow good performance to Li-O$_2$ batteries. Shao-Horn et al. [21] reported functionalized multiwall carbon nanotube/graphene composite with hierarchical pore structures serving as self-standing positive electrodes in lithium batteries. Electrode thicknesses up to tens of micrometers were achieved with a relatively high density (> 1 g/cm^3).

Toward free-standing carbon with micro and mesoscale pores, wood provides an ideal platform, offering macroscale structural integrity while presenting hierarchical pores inherent to its natural formation mechanism [25]. When carbonized appropriately, the structural integrity and the porosity can be preserved, yielding a carbon scaffold unique in its mechanical strength and structure [26]. Based on these considerations, we present a free-standing porous carbon derived from yellow pine [27]. To exploit the structured pores in wood enabled by microfibers and tracheids during the growth, we applied the resulting carbon as a cathode in Li-O$_2$ batteries, in which, the transport of a multitude of species is critically important [28]. Considering the discharge process as an example, O$_2$ (from the gas phase) is reduced and bound to Li$^+$ (from the liquid phase) to form Li$_2$O$_2$ (as a solid). The

process requires the transportation of O$_2$ from the headspace of the battery, Li$^+$ from the anode side through the electrolyte, and electrons from the cathode [29]. The concerted transportation of these three components requires a high surface area for large capacity, good electrical conductivity for high current density, and adequately large pores for the prevention of clogging [30]. All these requirements can be simultaneously satisfied by wood derived carbon. The channels and pores formed from the well-oriented microfibers and tracheids can serve as transport routes, through which a facile Li$^+$ and O$_2$ diffusion can be ensured. Preservation of the inherent structure of wood imparts adequate mechanical strength to carbon to be used as a free-standing electrode without excessive fabrication processes, eliminating the need for binders or conductive additives. Furthermore, we also explored the facile doping of N during the carbonization process, toward enhanced O$_2$ reduction reaction (ORR) activities [31, 32], which is critically important in the Li-O$_2$ battery operations.

2   Experimental

2.1   Material preparation

Pristine wood was obtained from yellow pine. The carbonization was carried out in two steps. As shown in Scheme 1, the wood was first cut into rectangular pieces and heated at 240 °C for 12 h in ambient air.
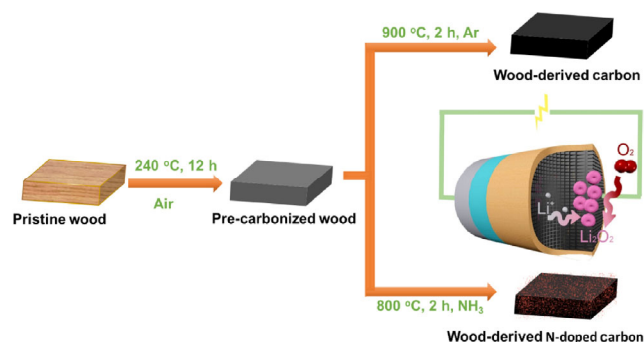
Scheme 1   Preparation of wd-C and wd-NC, and their application in Li-O$_2$ batteries. The wood was first cut into rectangular pieces and baked at 240 °C for 12 h in ambient air. For wd-C, the resulting sample was transferred to a tube furnace under an Ar atmosphere for complete carbonization at 900 °C for 2 h. For N-doped carbon (wd-NC), the carbonization was carried out at 800 °C with anhydrous NH$_3$ for 2 h.

The resulting sample was then transferred to a tube furnace under an Ar atmosphere (30 sccm (standard cubic centimeters per minute)) for complete carbonization at 900 °C for 2 h, to obtain wood-derived carbon (wd-C) [33].

For preparing N-doped carbon (wd-NC), carbonization was carried out at 800 °C, in the presence of anhydrous NH_3 (Airgas, 75 sccm), for 2 h. The wd-NC was not carbonized at 900 °C because wood was found to react vigorously with NH_3. The wd-C and wd-NC were further vacuum dried at 150 °C for at least 12 h in the antechamber, before transferring to the glovebox (Mbraun, MB20G, with O_2 and H_2O concentrations < 0.1 ppm). All the carbon samples with the areal density of 19 mg/cm^2 at the thickness of 1 mm were used directly without further processing.

2.2 Material characterization

Scanning electron microscopy (SEM) was performed on a JEOL 6340F microscope operating at 15 kV. Raman spectra were acquired from a micro-Raman system (XploRA, Horiba) using an excitation laser of λ = 532 nm. The surface area and pore volume were evaluated by N_2 adsorption/desorption experiments carried out at 77 K, using an automatic gas sorption analyzer (Autosorb iQ, Quantachrome). For X-ray photoelectron spectroscopic (XPS) analysis of the carbon electrode after Li-O_2 operations, the cell was transferred to an O_2-tolerant Ar-filled glovebox (H_2O level < 0.1 ppm, MBraun), and disassembled to extract the cathodes. The cathodes were further washed thrice with pure anhydrous dimethoxyethane (DME, anhydrous grade, Sigma-Aldrich) to remove trapped salts. Subsequently, they were vacuum-dried to remove solvents and transferred to the XPS (K-Alpha, Thermo Scientific) vacuum chamber with minimal exposure to ambient air (< 1 min). X-ray diffraction (XRD) data was obtained on a PANalytical X'Pert Pro diffractometer with an air-tight sample holder, without exposing the sample to ambient air. Mechanical tests were performed with a Discovery HR-1 hybrid rheometer. All test samples were of the same dimension (9 mm × 8 mm × 3 mm).

## 2.3 Electrochemical characterization

LiClO$_4$ (99.99%, battery grade, Sigma-Aldrich) was first baked at 130 °C in the antechamber of the glovebox and then dissolved in DME to obtain a 0.1 M electrolyte solution. Customized Swagelok™ type cells were assembled in the glovebox with Li metal (380 μm in thickness, Sigma-Aldrich) as the anode, 2 Celgard 2,400 film as the separator, and 0.1 M LiClO$_4$ (100 to 200 μL) as the electrolyte. The assembled batteries were then transferred to the O_2-tolerant Ar-filled glovebox and O_2 (ultrahigh purity, Airgas) was purged into the cell to replace Ar. Electrochemical characterizations were conducted using an electrochemical station (Biologic, VMP3).

3 Results and discussion

The free-standing nature of the wd-NC with good structural integrity can be visualized in Fig. 1(a). The mechanical properties of the resulting carbon were characterized by the engineering compression test. The ultimate loading stress before fracturing is shown in Fig. 1(b) and Fig. S1 in the Electronic Supplementary Material (ESM). For comparison, commercial Vulcan carbon (Vulcan-C) powder was molded into a similar size and shape but was bonded by 5% PVdF, which is commonly used as a cathode in literature [34]. As shown in Fig. 1(b), wd-NC bore the highest loading stress of 860 kPa. This clearly suggests that wd-NC features an adequate mechanical stability suitable for free-standing electrode applications.

During the first step of pre-carbonization, a 67% weight loss was measured corresponding to the dehydration and evaporation of small molecules. An additional 50% weight loss was observed during the second step for wd-C (i.e., the total weight of the
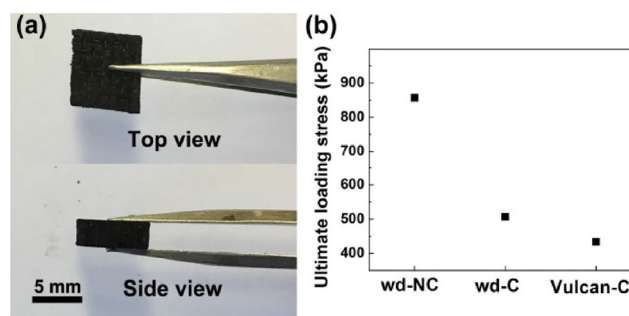
Figure 1 (a) Digital photographs showing the structural integrity of the freestanding wd-NC cathode. (b) A mechanical test comparison for wd-NC, wd-C, and Vulcan-C. wd-NC could bear the highest loading stress of 860 kPa.
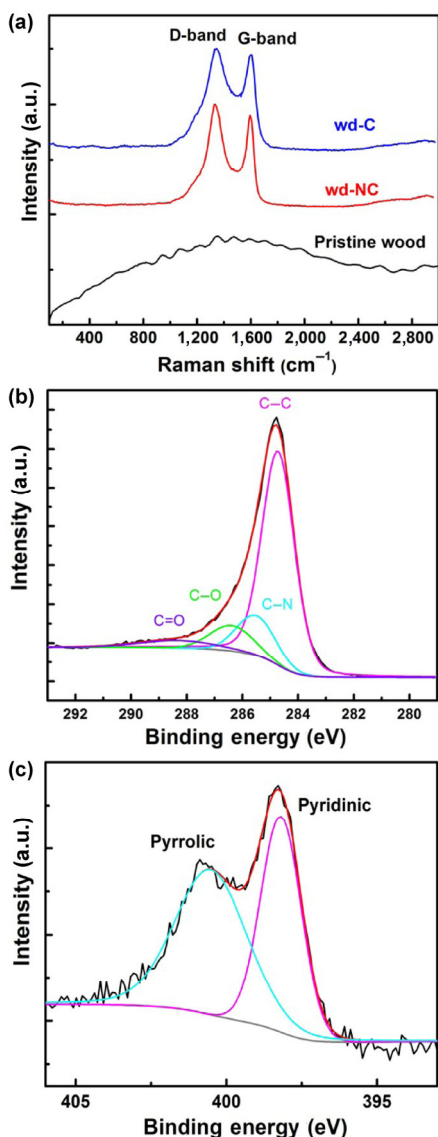
carbonized product is ca. 17% of the original wood weight). However, for wd-NC, the resulting substrate was measured to be only 11% of the original weight of the parent wood. The additional weight loss is a result of the reaction between carbon and NH_3 to form species such as HCN, C_2H_2, CH_3NH_2, and $CH_3C{\equiv}N$ [35]. This process activates the carbon material by enlarging the surface area and pore volume. Though some carbon is consumed in the process, the structural integrity of the wd-NC remains similar to that of wd-C. The microstructure of the resulting carbon materials was further characterized by SEM. Comparison of the microstructures of wd-C (Fig. 2(a)), wd-NC (Fig. 2(b)), and pre-carbonized wood (Fig. S3 in the ESM) indicates that the diameters of the channels are in the similar range of 10–50 μm. However, the micropore volumes of the two samples differed significantly (Fig. S2 and Table S1 in the ESM). The pore volume of wd-NC reached 0.36 cm^3/g, 10 times larger than that of wd-C. This difference can be rationalized by the aforementioned reaction between carbon and NH_3, which creates many more pores within the carbon structure. Figure 2(c) reveals that the hierarchical pore structure inherent to the parent wood remained intact, in which, channels enabled by the aligned microfibers penetrating through the
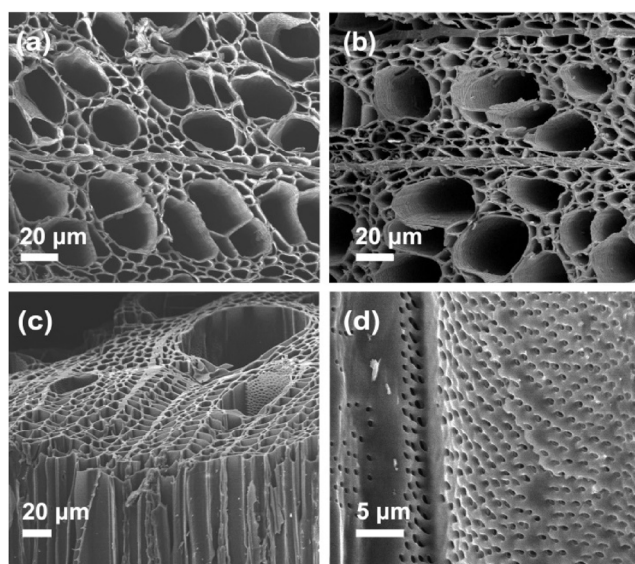
full thickness of the substrate formed the desired interconnected pathways for mass transport required in applications such as $Li-O_2$ batteries. In Fig. 2(d), a side-view image of the channel walls reveals the inter-channel pores on the walls of the carbon with an average diameter of 2 μm. These inter-channel pores are expected to further enable mass transport, by providing additional pathways in the event of pore clogging at the extremities of the channels.

Raman and XPS spectra were obtained to confirm the carbonization of wood and N doping. In the Raman spectra (Fig. 3(a)), the two peaks corresponding to the D-band at ~1,330 cm^{-1} and G-band at ~1,590 cm^{-1} [36] were prominent for both wd-C and wd-NC samples, whereas the pristine wood sample featured a severe fluorescence effect under illumination. The disappearance of the fluorescent behavior in the two carbon samples indicates the complete conversion from wood to carbon. The slightly higher D/G ratio of wd-NC sample indicates marginally poor crystallinity of the sample. While the difference may be reflected in the conductivity and stability of the cathode materials, the effect is expected to be negligible. The N content of wd-NC was further characterized by XPS. Figure 3(b) reveals the existence of carbon species in the form of C–C, C–N, C–O, and C=O. Semi-quantitative elemental analysis from XPS yielded 8% of N content on the surface of N-doped carbon and 9% O species. In comparison, XPS spectrum of wd-C did not show any N signal (Fig. S4 in the ESM). Further analysis of the N 1s spectrum (Fig. 3(c)) revealed the chemical environment of the doped N. The most prominent form appears to be pyridinic N represented by the peak with a binding energy of 398.2 eV [37]. This binding environment has been previously reported as the most active for the ORR. For example, Guo et al. [32] have shown that the carbon atoms next to pyridinic N are the active sites for O_2 adsorption, which is the initial step of ORR. In the same XPS spectrum (Fig. 3(c)), there is also a second peak corresponding to pyrrolic N at 400.7 eV. This is consistent with the N atom substituting the O atom in the 5-membered ring of the carbon precursor [37]. This analysis suggests that the doped N can potentially improve the ORR activity. Further details on this aspect will be discussed later in this article.

Figure 2 SEM images showing the microstructures of wd-C and wd-NC samples. (a) and (b) Top views of wd-C and wd-NC, respectively. (c) The hierarchical pore structure of wd-NC. (d) The inter-channel pores on the walls of wd-NC.

Figure 3 Raman and XPS characterizations confirming the carbonization and N doping of wd-NC (a) The two Raman peaks corresponding to the D-band at ~1,330 cm^{-1} and G-band at ~1,590 cm^{-1} of carbon are prominent for both wd-C and wd-NC samples. (b) The XPS spectrum of C 1s electrons, revealing the bonding environment of C in wd-NC. (c) The XPS spectrum of N 1s electrons, confirming the N doping in wd-NC and revealing the chemical environment of N. The most prominent component is the pyridinic N with the binding energy of 398.2 eV.

Next, we studied the electrochemical activity of the wood-derived freestanding carbon by incorporating it in Li-O_2 batteries, as a cathode material. First, we compared the performance of wd-NC with that of wd-C to investigate the effect of the hetero-atom (N atoms) on the Li-O_2 battery performance. As shown in Fig. 4, the discharge capacity for wd-NC is
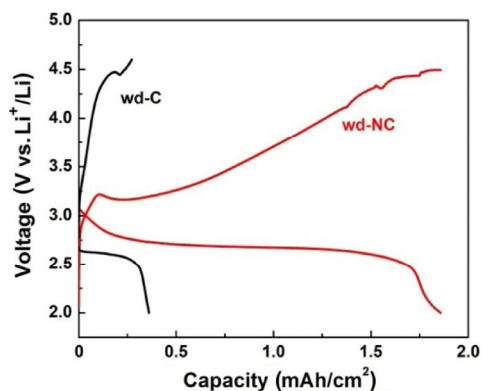

Figure 4 Voltage profiles of wd-NC and wd-C cathodes with the same current density of 0.08 mA/cm^2 (4 mA/g). Compared to wd-C, the average roundtrip overpotential of wd-NC decreased from 1.65 to 0.75 V and the areal capacity increased 5 times.

1.86 mAh/cm^2, ~5 times higher than that of wd-C (0.38 mAh/cm^2). The value is comparable to those measured for particulate carbon cathodes bonded by polymers (1–10 mAh/cm^2). The discharge potential increased from 2.55 (wd-C) to 2.70 V (wd-NC) as calculated from the plateau value of the discharge profile.

This phenomenon can be explained by the intrinsically high catalytic activity of the N-doped carbon, which is supported by previous experimental and computational studies [31, 32]. The NH$_3$ doping process can further activate the carbon by creating more micropores and enlarging the surface area. More significantly, the average recharge potential decreased from 4.20 to 3.45 V, suggesting that the discharge product may have a more intimate contact with the cathode, leading to more facile decomposition of Li$_2$O$_2$. Overall, the average overpotential of the charge/discharge process decreased from 1.65 to 0.75 V for wd-NC with 5 times increase in its capacity. The remarkable performance improvement further highlights the positive effect of N doping.

To demonstrate the practicality of the free-standing wd-NC cathode, we then characterized the test Li-O_2 battery cell at different charging/discharging rates. As shown in Fig. 5(a) and Fig. S5 in the ESM, as the current density varied between 0.04 and 0.20 mA/cm^2, the discharge voltage plateau decreased from 2.75 to 2.40 V, and the charge voltage plateau increased from 3.3 to 4.4 V. This indicates that the N doping facilitates the ORR kinetics more effectively than that of the oxygen evolution reaction (OER). Galvanostatic cycling
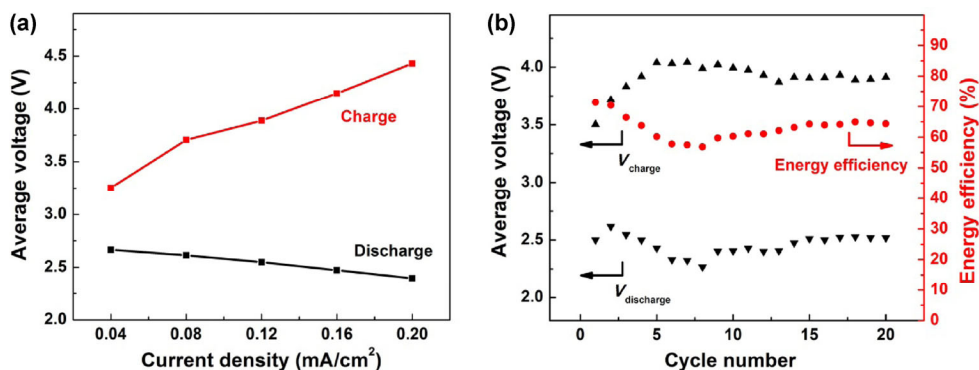
Figure 5 Rate capability and cycling performance of wd-NC. (a) Upon increasing the current density from 0.04 to 0.20 mA/cm², the discharge voltage plateau decreased from 2.75 to 2.40 V, and the charge voltage plateau increased from 3.3 to 4.4 V, indicating that the N-doping facilitates the ORR kinetics more effectively than that of the OER. (b) Galvanostatic cycling tests under a constant current density of 0.08 mA/cm² and 70% depth of full discharge (Absolute capacity of each cycle: 1.5 mAh). The average voltages and the energy efficiency for each cycle are plotted against the cycle number. The energy efficiency decreased from 70% to 60% after 5 cycles and remained stable afterwards.

tests were carried out under a constant current density of 0.08 mA/cm² (with the capacity being limited to 1.5 mAh, or 70% depth of full discharge). As presented in Fig. S6 in the ESM, for the first 20 cycles, the battery exhibited a stable discharge plateau of 2.5 V. However, the energy efficiency decreased from 70% to 60% after 5 cycles. Such poor stability of the carbon cathode has been observed by us as well as others [38]. We have previously shown that passivating the carbon cathode

or decorating it with catalysts or a combination of both processes could improve the cycling performance by reducing the parasitic chemical reactions [30].

Further, we analyzed the discharge and recharge products. This task is of paramount importance because proving that the electrochemical characteristics are indeed related to Li_2O_2 formation/decomposition is critical. For this, we conducted XRD characterizations. As shown in Fig. 6(a), the XRD pattern unambiguously
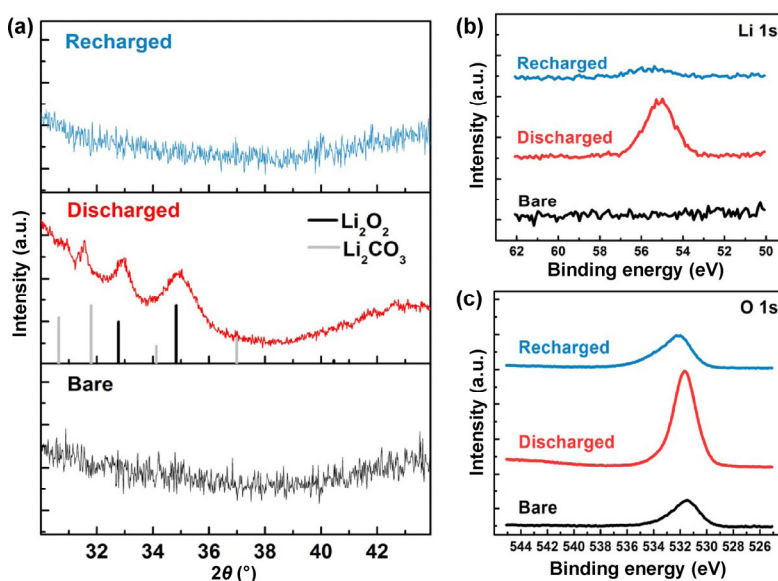
Figure 6 Li_2O_2 detection. (a) XRD patterns of wd-NC before discharge (bare), after the 1st cycle discharge (discharged) and the 1st cycle recharge (recharged). The peaks at 32.8° and 34.8° in the discharged sample match the documented diffraction peaks of Li_2O_2 (JCPDS 74-0115). (b) and (c) XPS spectra of Li 1s and O 1s confirming the formation and decomposition of Li_2O_2. After discharge, the peaks at 55.0 eV (Li 1s) and 531.8 eV (O 1s) increased dramatically, indicating the formation of Li_2O_2. After recharge, O 1s and Li 1s signal intensities decreased significantly, indicating the decomposition of Li_2O_2.

confirmed the formation of Li_2O_2 upon discharge. The peaks at 32.8° and 34.8° match the documented diffraction peaks of Li_2O_2 (JCPDS 74-0115). A shifted peak corresponding to the by-product Li_2CO_3 at 31.5° was also observed in the same XRD pattern. The slight shift (−0.3°) compared to the standard pattern (JCPDS 87-0729) is commonly observed for solution-derived samples [39], and is associated with the solvation of the Li^+ ions. XPS spectra were also collected to verify the composition of Li_2O_2 (Figs. 6(b) and 6(c)). After discharge, the peaks at 55.0 eV (Li 1s) and 531.8 eV (O 1s) increased dramatically, indicating the formation of Li_2O_2. After recharge, O 1s signal at 534.0 eV and Li 1s signal at 55.0 eV were observed with much lower intensities, indicating the decomposition of Li_2O_2 [40].

SEM images shown in Fig. 7 further support Li_2O_2 formation/decomposition. The surface of pristine wd-NC appears smooth and clean (Fig. 7(a)). After discharge, Li_2O_2 particles are observed to accumulate both within the pores and on the surface of the carbon walls (Fig. 7(b)). After a full recharge, these particles disappeared (Fig. 7(c)). The SEM images together with the XRD and XPS results strongly support that the formation and decomposition of Li_2O_2 correspond to the discharge and recharge electrochemical characteristics. A quantitative detection of Li_2O_2 by iodometric titration was not successful in this study [30, 41]. This is due to the large surface area and tortuosity of our free standing wood-derived N-doped carbon, resulting in the strong adsorption of iodine.

4   Conclusion

In summary, we investigated a new free-standing porous carbon material as a promising cathode material for Li-O$_2$ battery. This material takes advantage of the spontaneously formed hierarchical porous structures derived from wood. The structure is expected to facilitate both mass transport and discharge product storage. Moreover, we doped the heteroatom (N) to further improve the catalytic activity of the carbon cathode toward a lower overpotential and higher capacity. We have unequivocally confirmed that the initial electrochemical process involves the desired reactions of Li_2O_2 formation and decomposition. The free standing nature and the mechanical strength of wood-derived carbon aid in overcoming the need for additional current collectors and binders, thereby improving the overall energy density, and reducing possible parasitic chemical reactions. Moreover, the renewability of wood with its unique structure could potentially provide a cost-effective route for porous electrodes toward large-scale production. Further efforts to improve the cell performance can be anticipated by protecting the carbon surface using strategies previously demonstrated by us and others.
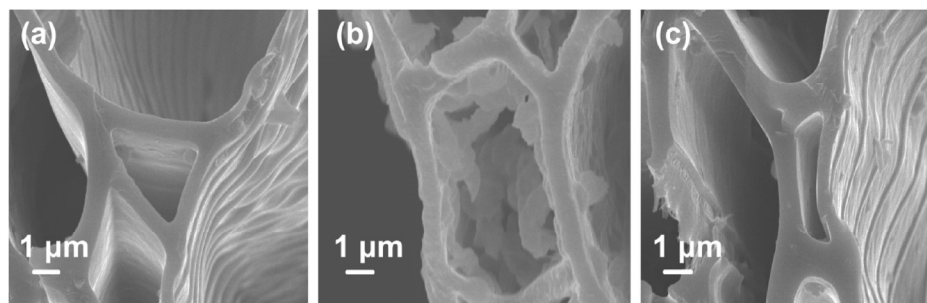
Figure 7   SEM images confirming the formation and decomposition of Li_2O_2. (a) Clean surface of bare wd-NC. (b) After discharge, the Li_2O_2 particles were observed to accumulate on the surfaces of wd-NC. (c) After the full recharge, the Li_2O_2 particles decomposed revealing the surface of the wd-NC.

Electronic Supplementary Material: Supplementary material (further details about mechanical test, surface area analysis and electrochemical data) is available in the online version of this article at https://doi.org/10.1007/s12274-017-1660-x.

References

[1] Fang, B. Z.; Kim, J. H.; Kim, M.; Yu, J. S. Ordered hierarchical nanostructured carbon as a highly efficient cathode catalyst support in proton exchange membrane fuel cell. *Chem. Mater.* **2009**, *21*, 789–796.

[2] Kjeang, E.; Michel, R.; Harrington, D. A.; Djilali, N.; Sinton, D. A microfluidic fuel cell with flow-through porous electrodes. *J. Am. Chem. Soc.* **2008**, *130*, 4000–4006.

[3] Long, J. W.; Dunn, B.; Rolison, D. R.; White, H. S. Three-dimensional battery architectures. *Chem. Rev.* **2004**, *104*, 4463–4492.

[4] Ogasawara, T.; Débart, A.; Holzapfel, M.; Novák, P.; Bruce, P. G. Rechargeable Li_2O_2 electrode for lithium batteries. *J. Am. Chem. Soc.* **2006**, *128*, 1390–1393.

[5] Wang, D. W.; Li, F.; Liu, M.; Lu, G. Q.; Cheng, H. M. 3D aperiodic hierarchical porous graphitic carbon material for high-rate electrochemical capacitive energy storage. *Angew. Chem., Int. Ed.* **2008**, *47*, 373–376.

[6] Zhai, Y. P.; Dou, Y. Q.; Zhao, D. Y.; Fulvio, P. F.; Mayes, R. T.; Dai, S. Carbon materials for chemical capacitive energy storage. *Adv. Mater.* **2011**, *23*, 4828–4850.

[7] Pandolfo, A. G.; Hollenkamp, A. F. Carbon properties and their role in supercapacitors. *J. Power Sources* **2006**, *157*, 11–27.

[8] Dutta, S.; Bhaumik, A.; Wu, K. C. W. Hierarchically porous carbon derived from polymers and biomass: Effect of interconnected pores on energy applications. *Energy Environ. Sci.* **2014**, *7*, 3574–3592.

[9] Long, C. M.; Nascarella, M. A.; Valberg, P. A. Carbon black vs. black carbon and other airborne materials containing elemental carbon: Physical and chemical distinctions. *Environ. Pollut.* **2013**, *181*, 271–286.

[10] Liu, G.; Zheng, H.; Song, X.; Battaglia, V. S. Particles and polymer binder interaction: A controlling factor in lithium-ion electrode performance. *J. Electrochem. Soc.* **2012**, *159*, A214–A221.

[11] Ha, D. H.; Islam, M. A.; Robinson, R. D. Binder-free and carbon-free nanoparticle batteries: A method for nanoparticle electrodes without polymeric binders or carbon black. *Nano Lett.* **2012**, *12*, 5122–5130.

[12] Chen, Z. H.; Li, H.; Tian, R.; Duan, H. N.; Guo, Y. P.; Chen, Y. J.; Zhou, J.; Zhang, C. M.; Dugnani, R.; Liu, H. Z.

Three dimensional graphene aerogels as binder-less, freestanding, elastic and high-performance electrodes for lithium-ion batteries. *Sci. Rep.* **2016**, *6*, 27365.

[13] Yao, X. H.; Dong, Q.; Cheng, Q. M.; Wang, D. W. Why do lithium–oxygen batteries fail: Parasitic chemical reactions and their synergistic effect. *Angew. Chem., Int. Ed.* **2016**, *55*, 11344–11353.

[14] Black, R.; Oh, S. H.; Lee, J. H.; Yim, T.; Adams, B.; Nazar, L. F. Screening for superoxide reactivity in $Li-O_2$ batteries: Effect on Li_2O_2/LiOH crystallization. *J. Am. Chem. Soc.* **2012**, *134*, 2902–2905.

[15] Amanchukwu, C. V.; Harding, J. R.; Shao-Horn, Y.; Hammond, P. T. Understanding the chemical stability of polymers for lithium–air batteries. *Chem. Mater.* **2015**, *27*, 550–561.

[16] Etacheri, V.; Sharon, D.; Garsuch, A.; Afri, M.; Frimer, A. A.; Aurbach, D. Hierarchical activated carbon microfiber (ACM) electrodes for rechargeable $Li-O_2$ batteries. *J. Mater. Chem. A* **2013**, *1*, 5021–5030.

[17] Lacey, M. J.; Jeschull, F.; Edström, K.; Brandell, D. Porosity blocking in highly porous carbon black by PVdF binder and its implications for the Li–S system. *J. Phys. Chem. C* **2014**, *118*, 25890–25898.

[18] Wang, Z. L.; Xu, D.; Xu, J. J.; Zhang, L. L.; Zhang, X. B. Graphene oxide gel-derived, free-standing, hierarchically porous carbon for high-capacity and high-rate rechargeable $Li-O_2$ batteries. *Adv. Funct. Mater.* **2012**, *22*, 3699–3705.

[19] Liu, Q. C.; Xu, J. J.; Xu, D.; Zhang, X. B. Flexible lithium-oxygen battery based on a recoverable cathode. *Nat. Commun.* **2015**, *6*, 7892.

[20] Xu, J. J.; Wang, Z. L.; Xu, D.; Zhang, L. L.; Zhang, X. B. Tailoring deposition and morphology of discharge products towards high-rate and long-life lithium-oxygen batteries. *Nat. Commun.* **2013**, *4*, 2438.

[21] Byon, H. R.; Gallant, B. M.; Lee, S. W.; Shao-Horn, Y. Role of oxygen functional groups in carbon nanotube/graphene freestanding electrodes for high performance lithium batteries. *Adv. Funct. Mater.* **2013**, *23*, 1037–1045.

[22] Yin, Y. B.; Xu, J. J.; Liu, Q. C.; Zhang, X. B. Macroporous interconnected hollow carbon nanofibers inspired by golden-toad eggs toward a binder-free, high-rate, and flexible electrode. *Adv. Mater.* **2016**, *28*, 7494–7500.

[23] Chang, Z. W.; Xu, J. J.; Liu, Q. C.; Li, L.; Zhang, X. B. Recent progress on stability enhancement for cathode in rechargeable non-aqueous lithium-oxygen battery. *Adv. Energy Mater.* **2015**, *5*, 1500633.

[24] Liu, T.; Liu, Q. C.; Xu, J. J.; Zhang, X. B. Cable-type water-survivable flexible $Li-O_2$ battery. *Small* **2016**, *12*, 3101–3105.

[25] Zhu, H. L.; Luo, W.; Ciesielski, P. N.; Fang, Z. Q.; Zhu, J. Y.; Henriksson, G.; Himmel, M. E.; Hu, L. B. Wood-derived materials for green electronics, biological devices, and energy applications. *Chem. Rev.* **2016**, *116*, 9305–9374.

[26] Zhu, H. L.; Jia, Z.; Chen, Y. C.; Weadock, N.; Wan, J. Y.; Vaaland, O.; Han, X. G.; Li, T.; Hu, L. B. Tin anode for sodium-ion batteries using natural wood fiber as a mechanical buffer and electrolyte reservoir. *Nano Lett.* **2013**, *13*, 3093–3100.

[27] Byrne, C.; Nagle, D. C. Carbonization of wood for advanced materials applications. *Carbon* **1997**, *35*, 259–266.

[28] Read, J.; Mutolo, K.; Ervin, M.; Behl, W.; Wolfenstine, J.; Driedger, A.; Foster, D. Oxygen transport properties of organic electrolytes and performance of lithium/oxygen battery. *J. Electrochem. Soc.* **2003**, *150*, A1351–A1356.

[29] Bruce, P. G.; Freunberger, S. A.; Hardwick, L. J.; Tarascon, J. M. Li–O$_2$ and Li-S batteries with high energy storage. *Nat. Mater.* **2012**, *11*, 19–29.

[30] Xie, J.; Yao, X. H.; Cheng, Q. M.; Madden, I. P.; Dornath, P.; Chang, C. C.; Fan, W.; Wang, D. W. Three dimensionally ordered mesoporous carbon as a stable, high-performance Li–O$_2$ battery cathode. *Angew. Chem., Int. Ed.* **2015**, *54*, 4299–4303.

[31] Gong, K. P.; Du, F.; Xia, Z. H.; Durstock, M.; Dai, L. M. Nitrogen-doped carbon nanotube arrays with high electrocatalytic activity for oxygen reduction. *Science* **2009**, *323*, 760–764.

[32] Guo, D. H.; Shibuya, R.; Akiba, C.; Saji, S.; Kondo, T.; Nakamura, J. Active sites of nitrogen-doped carbon materials for oxygen reduction reaction clarified using model catalysts. *Science* **2016**, *351*, 361–365.

[33] Pang, J.; John, V. T.; Loy, D. A.; Yang, Z.; Lu, Y. Hierarchical mesoporous carbon/silica nanocomposites from phenyl-bridged organosilane. *Adv. Mater.* **2005**, *17*, 704–707.

[34] Lu, Y. C.; Kwabi, D. G.; Yao, K. P. C.; Harding, J. R.; Zhou, J. G.; Zuin, L.; Shao-Horn, Y. The discharge rate capability of rechargeable Li-O$_2$ batteries. *Energy Environ. Sci.* **2011**, *4*, 2999–3007.

[35] Shevlin, P. B.; McPherson, D. W.; Melius, P. Reaction of atomic carbon with ammonia. The mechanism of formation of amino acid precursors. *J. Am. Chem. Soc.* **1983**, *105*, 488–491.

[36] Tuinstra, F.; Koenig, J. L. Raman spectrum of graphite. *J. Chem. Phys.* **1970**, *53*, 1126–1130.

[37] Matter, P. H.; Zhang, L.; Ozkan, U. S. The role of nano-structure in nitrogen-containing carbon catalysts for the oxygen reduction reaction. *J. Catal.* **2006**, *239*, 83–96.

[38] McCloskey, B. D.; Speidel, A.; Scheffler, R.; Miller, D. C.; Viswanathan, V.; Hummelshøj, J. S.; Nørskov, J. K.; Luntz, A. C. Twin problems of interfacial carbonate formation in nonaqueous Li–O$_2$ batteries. *J. Phys. Chem. Lett.* **2012**, *3*, 997-1001.

[39] Yin, W.; Grimaud, A.; Lepoivre, F.; Yang, C. Z.; Tarascon, J. M. Chemical vs. electrochemical formation of Li$_2$CO$_3$ as a discharge product in Li-O$_2$/CO$_2$ batteries by controlling the superoxide intermediate. *J. Phys. Chem. Lett.* **2017**, *8*, 214–222.

[40] Younesi, R.; Hahlin, M.; Björefors, F.; Johansson, P.; Edström, K. Li–O$_2$ battery degradation by lithium peroxide (Li$_2$O$_2$): A model study. *Chem. Mater.* **2013**, *25*, 77–84.

[41] Xie, J.; Dong, Q.; Madden, I.; Yao, X. H.; Cheng, Q. M.; Dornath, P.; Fan, W.; Wang, D. W. Achieving low overpotential Li–O$_2$ battery operations by Li$_2$O$_2$ decomposition through one-electron processes. *Nano Lett.* **2015**, *15*, 8371–8376.